Heat Mass Transfer (2013) 49:327–336
DOI 10.1007/s00231-012-1081-z

ORIGINAL

# Study of airflow in a cold-region tunnel using a standard $k - \varepsilon$ turbulence model and air-rock heat transfer characteristics: validation of the CFD results

**Xianjun Tan · Weizhong Chen · Guojun Wu · Jianping Yang**

Received: 8 January 2012 / Accepted: 8 October 2012 / Published online: 1 November 2012


**Abstract** An efficient computational fluid dynamics (CFD) method for simulating the flow and convective heat transfer process of airflow in a tunnel is required to analyze the freezing and thawing of surrounding rock and to apply the results to the design of the insulation layer for a tunnel located in a cold region. Comparisons of experimental data and CFD results using a standard $k - \varepsilon$ turbulence model, a wall function, a thermal function and an adaptive finite element method are presented. Comparison of the results indicated that the proposed model and simulation method are efficient at determining the solid–air interface heat coefficient in a thin and infinitely wide horizontal plate and the hydrodynamic and thermal fields in a 3-D cavity. After demonstrating that the necessary validations are satisfied, this paper presents an analysis of the characteristics of airflow and air–rock heat transfer in a cold-region tunnel.

## 1 Introduction

Permafrost, seasonally and instantaneously frozen soil (rock) occupies 50 % of the land on Earth. China is one of the largest countries with large cold regions that account for approximately 75 % of the country's total land area. With the increase in tunnel construction in cold regions, many problems involving frozen soil (rock) are encountered, These problems include freezing and thawing of rock surrounding tunnels. According to statistics, some of the tunnels in the northwest and northeast of China cannot be used for up to 8 or 9 months per year because of the damage caused by freezing and thawing, and transportation is negatively affected [18].

To address these problems, it is necessary to analyze the temperature field of the rock surrounding a tunnel. To date, research has been conducted that has focused on the temperature field in cold-region tunnels [33, 34]. In addition, because the water in the surrounding rock can have a great influence on the temperature distribution, several hydro-thermal (HT) and hydro-thermal-mechanical (THM) coupled models have been put forward [8, 13, 14, 19]. In our previous work, we established new governing equations for an HT coupling model and used these equations successfully to analyze the effect of insulation materials on the Galongla tunnel in the Tibet region of China [29]. However, it should be noted that none of these previous studies addressed the influence of tunnel ventilation. The airflow in a tunnel can significantly change the temperature of the surrounding rock, especially for tunnels in cold regions. This occurs because geothermal effects cause the air temperature inside a tunnel to be much higher than the air temperature outside the tunnel. When a tunnel is cut through, and because of the action of ventilation, heat will exchange intensively between the inside and outside of the tunnel, and between airflow and surrounding rock. Therefore, it is important to study the airflow in cold-region tunnels and their air-rock heat transfer characteristics.

### 1.1 Approaches available for tunnel airflow studies

There are two approaches to studying the airflow in tunnels: experimental measurements [5, 26] and computer

X. Tan (✉) · W. Chen · G. Wu · J. Yang
State Key Laboratory of Geomechanics and Geotechnical Engineering, Institute of Rock and Soil Mechanics, Chinese Academy of Sciences, Wuhan 430071, Hubei, China
e-mail: xjtan@139.com

W. Chen
Research Center of Geotechnical and Structural Engineering, Shandong University, Jinan 250061, Shandong, China

simulation [3, 6, 23, 25, 32]. Experimental measurements are reliable but require considerable effort and time, and typically only provide information for a few selected locations. Therefore, the experimental approach is not feasible as a routine design tool. A popular approach for computational simulation is the CFD method. However, popular models used in the CFD method to calculate turbulence typically require a fast computer with a large memory, so methods to simulate airflow have been studied by several researchers (e.g., [2, 7, 16].

### 1.2 Methods for numerical simulation of turbulent flows

Methods for numerical simulation of turbulent flows can be divided into three types: direct numerical simulation (DNS), large eddy simulation (LES), and the Reynolds-averaged Navier–Stokes (RANS) method.

DNS solves the highly reliable Navier–Stokes (N–S) equations without approximations. If this method can be applied successfully, it can obtain the smallest error results as well as an analytical solution, but this requires the grid resolution to be sufficiently fine. Anderson et al. [1] estimated that $10^5$ nodes must be arranged in 1 $cm^2$ to reflect turbulent flow characteristics, and it is obvious that the amount of computer storage space that is typically available at the present time is not adequate to satisfy this demand. Thus, except for the few researchers who have access to supercomputers for use in solving Navier–Stokes (N–S) equations to simulate simple turbulent flow by the DNS method, the more widespread successful application of DNS will depend on further improvements in computer processing speed and storage space.

According to eddy theory, turbulence is composed of eddies of many different sizes. Large-scale eddies mainly cause turbulence fluctuation and mixture, while small-scale eddies affect mainstream movement through nonlinear effects. Based on this understanding, the motion of large eddies can be simulate using unsteady N–S equations, and the influence of small eddies on large eddies can be considered using an approximate model. Because this approach neglects many details of small eddies in the computational process, and only the movements of large eddies are simulated, the computational time and space requirements are greatly reduced, compared to the DNS method. The LES method has developed rapidly in recent decades [11, 21, 28].

The RANS method solves ensemble-averaged N–S equations using turbulence modeling. In the last two decades, many numerical model based on the RANS method have been developed, such as the standard $k-\varepsilon$ model and algebraic and differential Reynolds stress models [7]. The standard $k-\varepsilon$ model was used in this study because it is easy to program and gives reasonable results in many applications.

### 1.3 Convective heat transfer coefficient (CHTC)

The CHTC is not only the key boundary condition in the calculation of the temperature distribution of rock surrounding a tunnel, but is also an important parameter in establishing the required thickness of heat insulation material. Wijeysundera et al. [31] determined that an error of 15 % in the convection heat transfer coefficient will lead to an error of approximately 15–20 % in heat flow prediction. Thus, analysis of heat exchange between airflow and surrounding rock requires knowledge of the CHTC, which can be defined as follows:

$$h = \frac{q}{(T_s - T)} \tag{1}$$

where $h$ is the CHTC ($W/m^2$ K), $q$ is the convective heat flux density ($W/m^2$), $T_s$ is the surface temperature of the surrounding rock, and $T$ is the temperature of the airflow.

For the forced convection in a tunnel, the CHTC is usually correlated to the wind speed at a reference location. Linear or power law correlations are usually reported. These correlations can be obtained by wind tunnel experiments or full-scale experiments [12, 22, 24]. Another option to obtain the CHTC is to use CFD [9, 23]. The main advantages of CFD are that high-Reynolds-number flows for atmospheric conditions can be considered and, apart from the flow field, detailed information about the thermal field can be obtained, which is valuable for the analysis of the CHTC. Conducting an in situ experiment in a tunnel is difficult, so in this study, the CFD method is adopted to establish the CHTC, and the logarithmic wall function boundary condition for turbulent flow is used to model solid–air interfaces [17].

The purpose of this paper is to present the development of a turbulent flow model and put forward an efficient CFD method (see in Fig. 1) that is suitable for use in characterizing the airflow in a cold-region tunnel and that can reflect the heat exchange regularity between air and surrounding rock. This paper is organized as follows. The details of the governing equations for the numerical simulations are described in Sect. 2. Then, two different configurations are analyzed. The first configuration is a horizontal stream of air that cools a thin and infinitely wide horizontal plate (Sect. 3). This configuration is used to validate the accuracy of the numerical predictions of CHTC by the CFD method, which is performed by comparison with an empirical formula. The second configuration is a cube cavity (Sect. 4). The purpose of this section is to validate that the proposed model and simulation method are efficient at solving the hydrodynamic and thermal fields. In Sect. 5, conclusions are given.

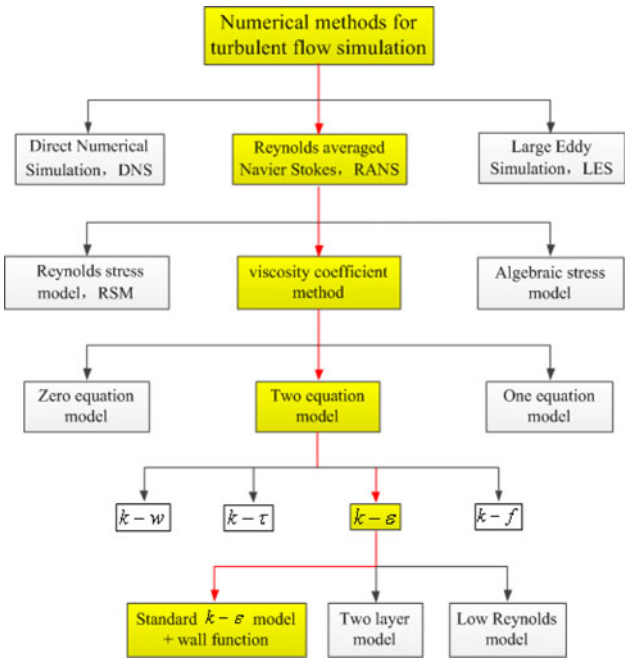


**Fig. 1** Methods for numerical simulation of turbulent flows (the *yellow*-highlighted methods are those chosen for use in this study)

## 2 Governing equations

The governing equations to be considered are the time-averaged continuity, momentum, and energy equations. Hence, the governing equations for the airflow region can be written as follows.

### 2.1 Time-averaged continuity equation

$$\nabla \cdot (\rho \mathbf{u}) = 0 \tag{2}$$

where $\mathbf{u}$ is the velocity and $\rho$ is the density, which can be established by the ideal gas state equation.

### 2.2 Time-averaged momentum equation (N–S equation)

$$\nabla \cdot (\rho \mathbf{u})\mathbf{u} = \nabla \cdot \left[ -p\mathbf{I} + (\mu + \mu_{\mathrm{t}}) \times \left( \nabla \mathbf{u} + (\nabla \mathbf{u})^{\mathrm{T}} - \frac{2}{3}(\nabla \cdot \mathbf{u})\mathbf{I} \right) - \frac{2\rho k}{3}\mathbf{I} \right] + \mathbf{S_M} \tag{3}$$

where $p$ is the pressure, $\mu$ is the viscosity coefficient, $\mathbf{I}$ is the unit matrix, $\mu_{\mathrm{t}}$ is the eddy viscosity coefficient, $\mathbf{S_M} = \rho\mathbf{X} - \frac{\partial}{\partial x}(\mu' \nabla \cdot \mathbf{u})$, $\mathbf{X}$ is the body force along with coordinate axis orientation and $\mu'$ is the second viscosity coefficient, which is usually assumed to be equal to $\mu' = \frac{2}{3}\mu(\nabla \cdot \mathbf{u})$ for gas.

### 2.3 Time-averaged heat transfer equation

$$\nabla \cdot (\rho c_{\mathrm{p}} \mathbf{u} T) = \nabla \cdot \left[ \left( \lambda_{\mathrm{g}} + c_{\mathrm{p}} \frac{\mu_{\mathrm{t}}}{\mathrm{Pr_T}} \right) \nabla T \right] + Q_{\mathrm{T}} \tag{4}$$

where $c_{\mathrm{p}}$ is the specific heat, $\lambda_{\mathrm{g}}$ is the conductivity, $\mathrm{Pr_T}$ is the turbulence Prandtl number and $Q_{\mathrm{T}}$ is the heat source.

### 2.4 $k - \varepsilon$ two-equation turbulence model

The turbulence kinetic energy $k$ and its rate of dissipation $\varepsilon$ are governed by the following transport equations:

$$\begin{cases} \nabla \cdot (\rho k)\mathbf{u} = \nabla \cdot \left[ \left( \mu + \frac{\mu_{\mathrm{t}}}{\sigma_{\mathrm{k}}} \right) \nabla k \right] + \mu_{\mathrm{t}} P(\mathbf{u}) - \frac{2\rho k}{3} \nabla \cdot \mathbf{u} - \rho\varepsilon \\ \nabla \cdot (\rho\varepsilon)\mathbf{u} = \nabla \cdot \left[ \left( \mu + \frac{\mu_{\mathrm{t}}}{\sigma_{\varepsilon}} \right) \nabla \varepsilon \right] + \frac{C_{\varepsilon 1}\varepsilon}{k} \left[ \mu_{\mathrm{t}} P(\mathbf{u}) - \frac{2\rho k}{3} \nabla \cdot \mathbf{u} \right] - \frac{C_{\varepsilon 2}\rho\varepsilon^2}{k} \end{cases} \tag{5}$$

where $P(\mathbf{u}) = \nabla \mathbf{u} : [\nabla \mathbf{u} + (\nabla \mathbf{u})^{\mathrm{T}}] - \frac{2}{3}(\nabla \cdot \mathbf{u})^2$ and the eddy viscosity coefficients are expressed as follows:

$$\mu_{\mathrm{t}} = \frac{\rho C_{\mu} k^2}{\varepsilon} \tag{6}$$

where $\sigma_{\mathrm{k}}$, $\sigma_{\varepsilon}$, $C_{\varepsilon 1}$, $C_{\varepsilon 2}$, and $C_{\mu}$ are empirical constants.

### 2.5 Boundary conditions

#### 2.5.1 *Logarithmic wall functions*

Turbulence close to a solid wall is very different from isotropic free-stream turbulence. This must be accounted for in a proper model [20]. There are basically two approaches to account for turbulent flow near solid walls. The first approach, used for low-Reynolds-number turbulence models, modifies the equations by additional terms and factors that account for near-wall effects. In such a case, the mesh must be refined near the wall to resolve the viscous sublayer. Sometimes, this may require as many as 20–30 nodes, the solution for which is often difficult to obtain by engineering calculation, so such methods are of interest for moderate Reynolds numbers, where near-wall resolution leads to a more reasonable number or elements. In the second approach, which we have used, an empirical relation between the value of velocity and wall friction replaces the thin boundary layer near the wall. Such relations are known as wall functions and are accurate for high Reynolds numbers and situations where pressure variations along the wall are not very large. The difference in space discretization is schematically depicted in Fig. 2.

Logarithmic wall functions applied to finite elements assume that the computational domain begins a distance $y$ from the real wall, and they also assume that the flow is

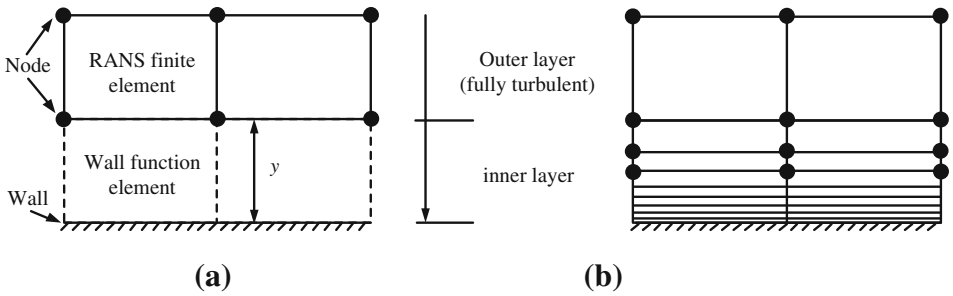


**Fig. 2** Different discretizations of the computational domain close to a wall. **a** Mesh for wall function. **b** Mesh for low-Reynolds-number turbulence models

parallel to the wall and that the velocity scale $u^*$ can be described as follows:

$$u^* = \sqrt{\tau_w/\rho} \tag{7}$$

where $\tau_w$ is the wall shear stress.

The following definition provides a velocity scale based on the turbulence kinetic energy:

$$u^* = C_\mu^{\frac{1}{4}} k^{\frac{1}{2}} \tag{8}$$

The definitions of $u^+$ and $y^+$ are then:

$$u^+ = u/u^* \tag{9}$$

$$y^+ = yu^*\rho/\mu \tag{10}$$

and the relationship between $u^+$ and $\delta_w^+$ can be described as follows:

$$u^+ = \frac{1}{\kappa}\ln(y^+) + C^+ \tag{11}$$

Substituting Eqs. (8), (10) and (11) into Eq. (9), the relationship between velocity and the distance $y$ from the real wall can be expressed as follows:

$$u = \left[\frac{1}{\kappa}\ln\left(\frac{\rho C_\mu^{\frac{1}{4}} k^{\frac{1}{2}} y}{\mu}\right) + C^+\right] C_\mu^{\frac{1}{4}} k^{\frac{1}{2}} \tag{12}$$

With the near-wall velocity for high-Reynolds-number turbulence solved, the next two remaining variables $k$ and $\varepsilon$ in this region can be solved as follows:

Because $k$ is close to zero near a wall, the equation for $k$ can be solved with a zero-gradient wall boundary condition.

Because $\varepsilon$ approaches infinity near a wall, an empirical expression for $\varepsilon$ was used, which is given by the following:

$$\varepsilon = \frac{C_\mu^{3/4} k^{3/2}}{\kappa y} \tag{13}$$

### 2.5.2 Thermal wall function

The logarithmic wall function boundary condition for turbulent flow is used to model the solid–air interfaces. An algebraic relationship—the logarithmic wall function—describes the momentum transfer at the solid–air interface. This means that the solid–air boundaries in the model actually represent lines within the logarithmic regions of the boundary layers. As with the airflow velocity, the temperature is not modeled in the innermost part of the boundary layer. Instead of assuming continuity of the temperature across the layer, a thermal "wall function" is used. There is a jump in temperature from the solid surface to the airflow due to the omitted innermost part of the boundary layer. To obtain the thermal wall function, the model uses two heat transfer application modes: one for the solid and one for the air. These are connected through a heat flux boundary condition, the thermal wall function. This means that the resistance to heat transfer through the innermost part of the boundary layer is related to that for momentum transfer for the air. The heat flux, $q$, is determined from the following equation.

$$q = \frac{\rho c_p C_\mu^{1/4} k^{1/2}}{T^+}(T_s - T) \tag{14}$$

where $\rho$ and $c_p$ are the air's density and heat capacity, respectively; $C_\mu$ is a constant of the turbulence model; and $k$ is the value of the turbulent kinetic energy at the wall. $T_s$ is the temperature of the solid at the wall, while $T$ is the temperature of the air on the other side of the omitted laminar sublayer. The dimensionless quantity $T^+ = T^+(y^+)$ is the dimensionless temperature and depends on the dimensionless wall offset, $y^+$. The relations are given in Comsol as follows:

$$T^+ = \begin{cases} \Pr y^+ & y^+ < y_1^+ \\ 15\Pr^{2/3} - 500/(y^+)^2 & y_1^+ \le y^+ < y_2^+ \\ \ln(y^+)\Pr/\kappa + \beta & y^+ \ge y_2^+ \end{cases} \tag{15}$$

with the following definitions:

$$\begin{cases} y_1^+ = \frac{10}{\Pr^{1/3}} \\ y_2^+ = 10\sqrt{10\frac{\kappa}{\Pr_T}} \\ \beta = 15\Pr^{2/3} - \frac{\Pr_T}{2\kappa}\left[1 + \ln\left(1000\frac{\kappa}{\Pr_T}\right)\right] \end{cases} \tag{16}$$

From Eq. (11), the CHTC can be obtained:

$$h = \frac{\rho c_p C_\mu^{1/4} k^{1/2}}{T^+} \tag{17}$$

The advantage of this method is that as long as parameters for the turbulence model are determined, heat flux between solid and air can be obtained without extra testing and assumptions.

### 2.6 Numerical methods

Commercial finite element software, COMSOL Multiphysics (version 4.2), was used in this study to implement all of the models and for all of the numerical simulations. The RANS models used the second-order upwind scheme for all of the variables except pressure. The discretization of pressure is based on a staggered scheme. The SIMPLE algorithm is adopted to couple the pressure and momentum equations. If the sum of the absolute normalized residuals for all elements becomes less than $10^{-6}$ for energy and $10^{-3}$ for other variables, the solution is considered converged. The adaptive FEM and the grid dependence of each case are checked using two to four different grids to ensure that grid resolution would not have a notable impact on the results.

## 3 Thermal wall function method validation study

Figure 3 depicts the geometry modeled: a horizontal stream of air cools a thin and infinitely wide horizontal plate. The plate is at a uniform temperature at the bottom, and the flow is turbulent. This is a well-studied case of convection cooling that works well as a benchmark that demonstrates the accuracy of the modeling methods.

The basis of the model for CFD calculation is shown in Fig. 3, and the position $x = 0$ is the leading edge of the heated part of the horizontal plate. The boundary conditions are set as follows: the temperature of the plate is 120 °C; the upper limit is a symmetry boundary; the inlet velocities of the left boundary are 1, 5, 10 and 20 m/s; the temperature is 20 °C; and the right boundary is the exit boundary. The CHTC between the airflow and the horizontal plate is obtained by two methods for comparison. One method adopts a thermal wall function, and the other method adopts an empirical formula suggested by Bejan [4], in which the CHTC is expressed as follows:

$$h = \left(\frac{k}{L}\right) 0.0296 \, \mathrm{Pr}^{0.38} \, \mathrm{Re}^{0.8} \tag{18}$$

The other calculation parameters for CFD calculation are shown in Table 1.

Figure 4 shows the local heat transfer coefficient as determined empirically (solid) and with the thermal wall function (dashed) for various inlet velocities. From this figure, it can be observed that the model agrees well with empirical data for low to intermediate inlet velocities. However, at high inlet velocities, the results do not match quite as well due to the model used for the flow, especially at the leading edge of the plate. This is because the thermal wall function is valid under certain conditions that depend on the resolution, the velocity and the viscosity. For the wall function to be an accurate approximation, $y+$ for the first internal node should be greater than 30 but less than some upper limit dependent on the Reynolds number. When the inlet velocity is 20 m/s or more, the mesh is a bit too coarse for this case. As a consequence, the heat transfer coefficient becomes less accurate. We can easily correct this situation by making the mesh finer at the boundary at the leading edge of the plate.

Figure 5 is the whole model of air and hot plate temperature distribution when the wind speed is 20 m/s and the air temperature is 20 °C. The heating effect of the hot horizontal plate on the air can be observed clearly.

## 4 Turbulent flow in a cube cavity

### 4.1 Description

A classic anisothermal ventilated cavity laboratory experiment was investigated by Blay et al. [5]. Although the configuration is a laboratory model rather than a real-sized room, the induced mixed convection flow inside this cavity is representative of flow features found in real rooms and is numerically very challenging, so the results were adopted by many researchers [10, 32]. The experimental database includes charts of the mean values of velocity, temperature and turbulent kinetic energy in the mid-depth plane of the cavity and is well suited for CFD code validation. Here we use these experimental results to verify the validation of the proposed model for simulating turbulent airflow including solid–air thermal exchange.

The geometry of the experimental cavity is shown in Fig. 6. The length, width and height of the cavity are

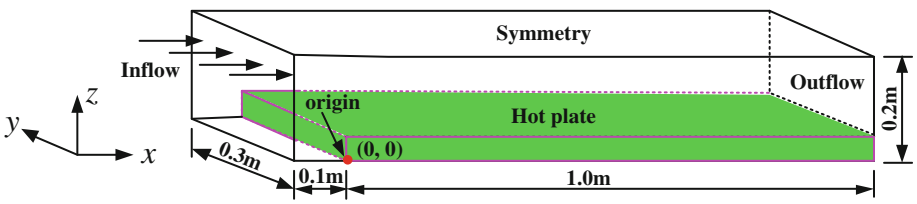


**Fig. 3** Forced convection cooling of a *horizontal plate*

**Table 1** Empirical parameters for the $k - \varepsilon$ model

| Pr | $Pr_T$ | $C_\mu$ | $\sigma_k$ | $\sigma_\varepsilon$ | $C_{\varepsilon 1}$ | $C_{\varepsilon 2}$ | $\kappa$ |
|---|---|---|---|---|---|---|---|
| 0.7 | 1.0 | 0.09 | 1.0 | 1.3 | 1.44 | 1.92 | 0.42 |

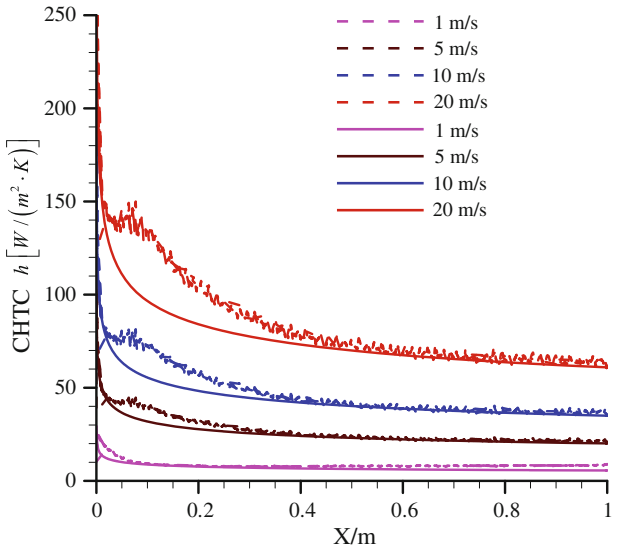


**Fig. 4** CHTC as determined empirically (*solid*) and with the model (*dashed*) for various inlet velocities

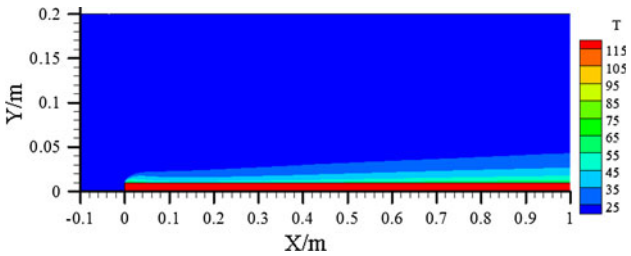


**Fig. 5** The temperature field at an inlet velocity of 20 m/s (unit: °C)

$L = 1.04$ m, $W = 0.7$ m, and $H = 1.04$ m, respectively. Airflow blows into the experimental cavity from a thin inlet slot with a height of $h_{in} = 0.018$ m and a velocity of $\mathbf{u}_{in} = 0.57$ m/s and a temperature $T_{in} = 15$ °C, and exits through a thin slot with a height of $h_{out} = 0.024$ m at the opposite wall. The two slots extend through the whole width of the cavity. The experimental cavity had a floor heating system that kept the floor temperature at $T_f = 35$ °C, while the temperature of the ceiling and the two opposite lateral walls was maintained at $T_w = 15$ °C. The corresponding Archimedes number $A_r = 0.0036$ and the Reynolds number $Re = 678$. The turbulence intensity $I_T$ is 6 %, and the turbulent length scale, $L_T$, is 0.148.

Mesh properties are very important to accurate analysis with the FEM. It is important to select a mesh that minimizes errors in the quantities of interest. A smooth tangent-hyperbolic law is applied for the distributions along the $X$,

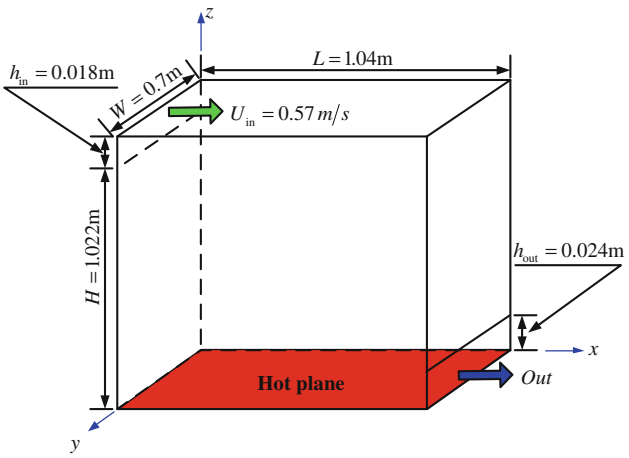


**Fig. 6** Schematic representation of the experimental cavity

$Y$ and $Z$ directions to refine the mesh near the walls as well as inside the inlet and the outlet regions. The position of the first inner grid point in the X direction is $1 \times 10^{-3}$ in non-dimensional units. In addition, an adaptive finite element technology is adopted to obtain a sufficiently accurate solution. This approach has been demonstrated to produce very accurate and high-quality solutions to a wide variety of problems [15, 17, 27, 30].

The boundary conditions are specified as follows:

Inlet boundary conditions:

$$\mathbf{u} = \mathbf{u}_{in} = 0.57 \text{ m/s}, k = \left(3I_T^2/2\right)(\mathbf{u}_{in} \cdot \mathbf{u}_{in}),$$

$$\varepsilon = C_\mu^{0.75} k^{3/2} \Big/ L_T, T = T_{in} = 15\,^\circ\text{C}$$

where $\mathbf{u}_{in}$ is the inlet velocity, $I_T$ is the turbulence intensity and $L_T$ is the turbulent length scale.

Adiabatic wall boundary conditions:

$$\mathbf{u} = 0, T = 15\,^\circ\text{C}$$

Interfacial boundary conditions:

$$-\text{n} \cdot \left[\left(\lambda_g + c_p \frac{\mu_t}{Pr_T}\right)\nabla T\right] = h(T_s - T)$$

$$h = \frac{\rho c_p C_\mu^{1/4} k^{1/2}}{T^+}$$

Exit boundary conditions:

$$p = p_{atm}, -\text{n} \cdot \left[\left(\lambda_g + c_p \frac{\mu_t}{Pr_T}\right)\nabla T\right] = 0$$

The values of the other parameters are given in Table 1.

## 4.2 Results

Based on the available experimental data, only the median plane of the cavity ($y = 0.35$) will be considered. Blay et al. measured the average velocity distribution with the

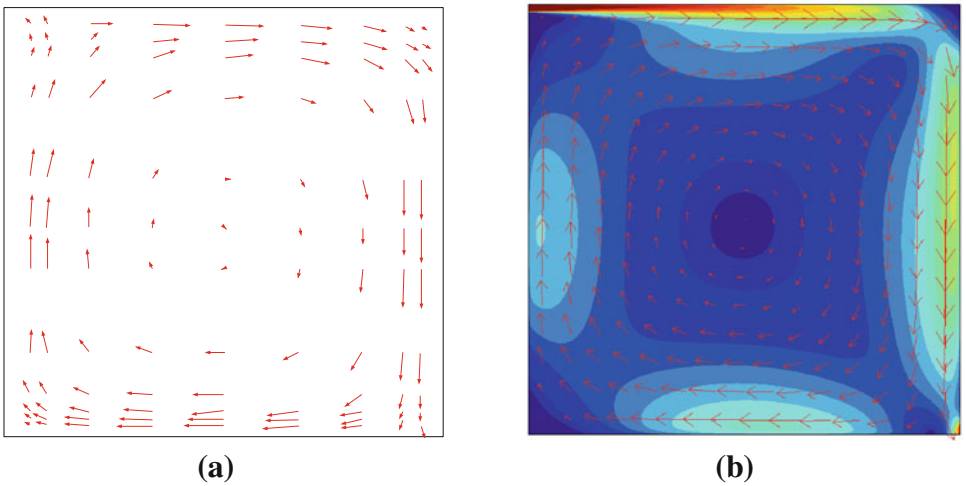


**Fig. 7** Average velocity vector diagram. **a** The experiment result. **b** The simulation result

apparatus shown in Fig. 7a. With the turbulence model proposed in this paper, the average velocity is calculated using the FEM shown in Fig. 7b. The air transport model results shown in the two figures are basically consistent.

Although the experimental results and the present $k - \varepsilon$ model do not show recirculation, Chen [7] reported that none of the five $k - \varepsilon$ models he tested was able to predict recirculation. Zhang and Chen [32] observed recirculation in the upper right corner and in the lower left corner of the cavity. LES by Ezzouhri et al. [10] showed recirculation cells in a counterclockwise rotation case. It is not clear whether this is due to insufficiently fine measuring points or due to the model used or due to insufficient resolution near the wall. One explanation maybe that the wall function approach gives reasonably accurate predictions for the majority of high-Reynolds-number, wall-bounded flows, but becomes less reliable when the flow conditions depart from the ideal conditions underlying the wall functions. For example, the standard wall functions do not account for the effects of pressure gradients, nor for departure from equilibrium, nor for massive transpiration through the wall (blowing/suction). However, from the latter study it can be observed that the proposed model can simulate the experimental results exactly, and much excellent research has been performed on the wall function approach [17]. Because no unified understanding is available, it is difficult to identify the actual cause of the discrepancies.

The velocity distribution obtained from the FEM is shown in Fig. 8. From Fig. 8, it can be observed that air in this model rotates under the action of inlet air. The air velocity in the center and at the corners of the model is low. However, the air velocity at the center of each side wall is much higher. The temperature distribution obtained from the FEM is shown in Fig. 9. From this figure, it is concluded that the wind flow has a great influence on the temperature distribution.

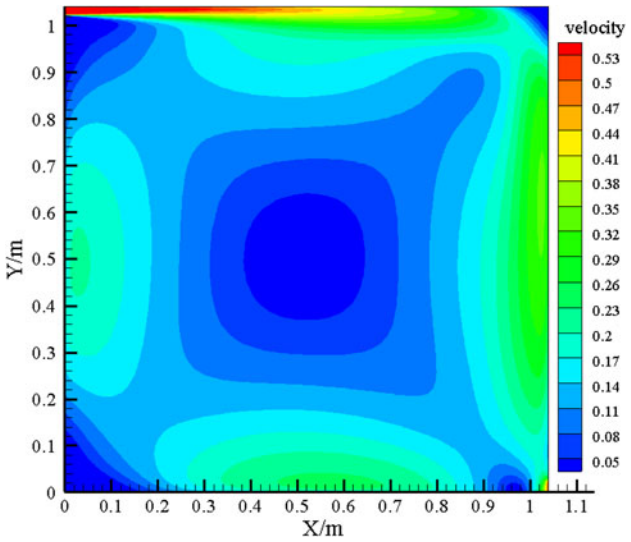


**Fig. 8** Velocity distribution (units: m/s)

To present the distributions of wind velocity and temperature in this model, the calculation results and measurements of average velocity and temperature in different sections at mid-width ($y = 0.35$) are shown in Figs. 10, 11, 12 and 13.

We compare the results obtained not only with the experimental results [5] but also with the LES results from the recent comparative study of different CFD approaches conducted by Zhang and Chen [32]. They used the FLUENT commercial code for their simulations and a filtered dynamic subgrid-scale model (FDSM) approach for their LES results on a $60 \times 30 \times 60$ grid point mesh. In addition, they used the Smagorinsky model (SM) ($C_S = 0.16$) for comparison. All of the results were used for comparison in this study.

Figures 10 and 11 show that the present model and the two subgrid-scale models yield very similar air velocity profiles. The predicted velocity profiles agree reasonably

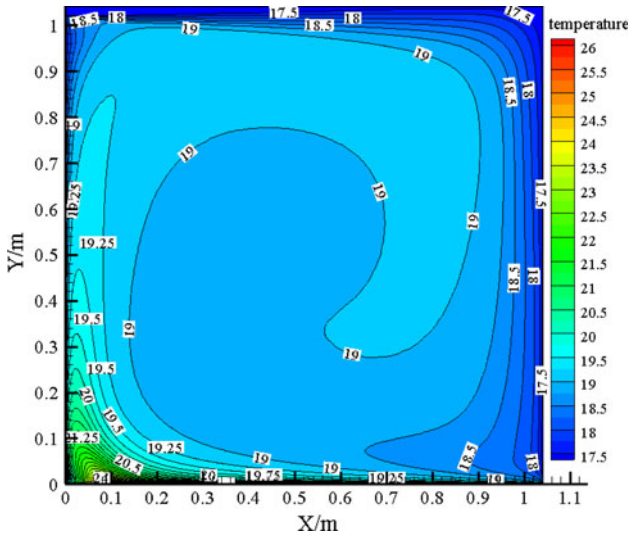


**Fig. 9** Temperature distribution (units: °C)

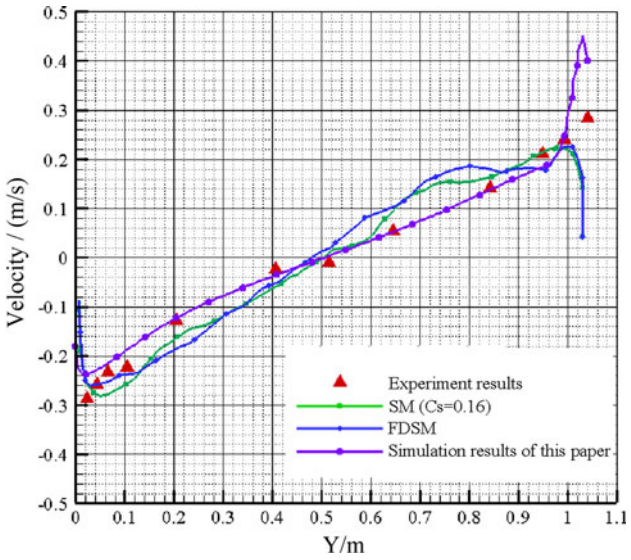


**Fig. 11** Velocity distribution at $x = 0.52$ m section

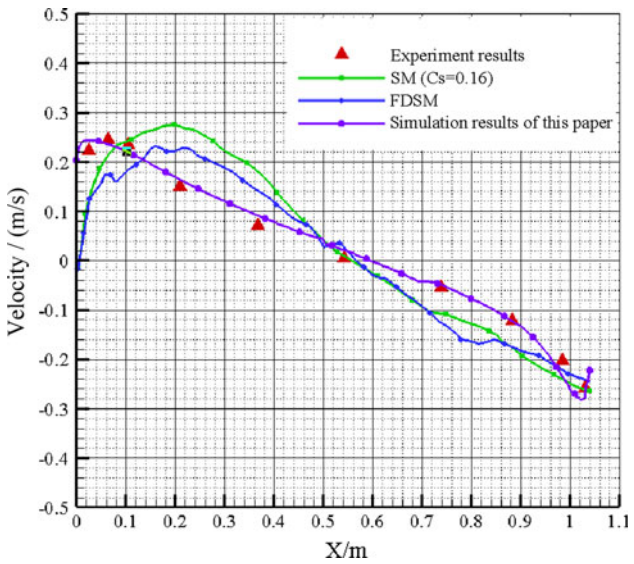


**Fig. 10** Velocity distribution at $z = 0.52$ m section

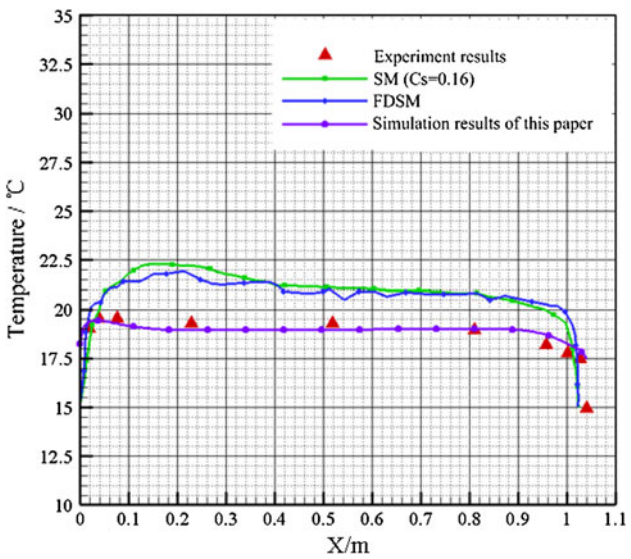


**Fig. 12** Temperature distribution at z = 0.52 m section

with the experimental data. However, some differences can be observed between our results and those of Zhang and Chen [32] in Figs. 11 and 12. Zhang and Chen [32] predicted a very narrow ceiling jet. Our results, on the other hand, indicate a slight overprediction of the peak velocity value. The calculated peak value of average velocity at the surface of the side wall in the section with $x = 0.52$ m is higher than the measured peak value. The main reason for this phenomenon may be that the peak value was not measured because of limitations on the sensor locations and number.

From Figs. 12 and 13, it can be observed that the temperature distribution and curve shape in certain sections in the research results from our model and from Zhang and Chen [32] are basically consistent with the measured results. However, the calculated temperature at each point in the model is approximately 1.7 K higher than the measured value, including the peak value of temperature. Perhaps because in their analysis the computations did not use a wall function for the solid boundaries, the models may overpredict the heat transfer from the floor or underpredict the heat transfer to the other walls, or the Prandtl number of the subgrid scale may not be correctly modeled. Because no detailed measurements on the heat transfer are available, it is difficult to identify the actual cause of the discrepancies. Using the calculation model and parameters

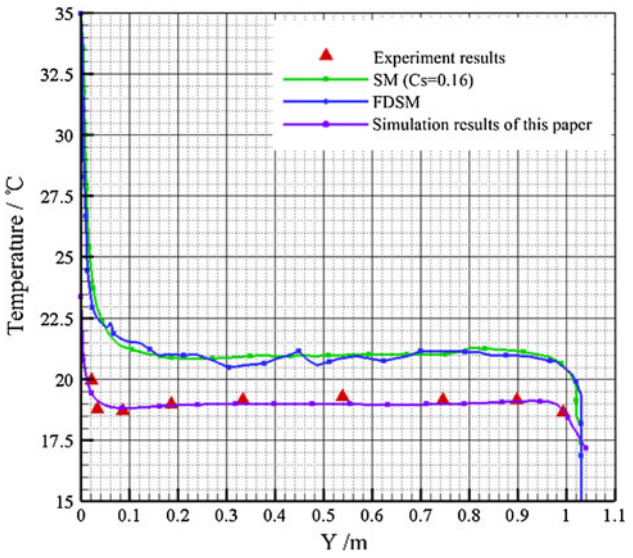


**Fig. 13** Temperature distribution at $x = 0.52$ m section

from this study, the calculation results are consistent with the measurement results, and these results were verified in the research work of Ezzouhri et al. [10].

## 5 Conclusions and discussions

The main objective of this study was to investigate an efficient CFD method to simulate the flow and convective heat transfer process of airflow in a cold-region tunnel. The computed results were compared with those of the FDSM, the SM and the experimental data available from the literature. From the comparisons, that the following conclusions are drawn:

- The thermal wall function results agree well with empirical data for low to intermediate inlet velocities; however, at high inlet velocities, the results do not match quite as well, due to the flow model. It may be possible to correct this situation by making the mesh finer at the boundary.
- The proposed model with the standard $k - \varepsilon$ turbulence model, wall function, thermal function and adaptive FEM can predict the mean flow parameters, such as mean air velocity and temperature, well.
- The purpose of this paper was to investigate an efficient CFD method to simulate the flow and convective heat transfer process of airflow in a cold-region tunnel, so only the experimental condition was studied. Although results for different Reynolds numbers were investigated in previous research (e.g., [10]), we can do some investigation of the same using our proposed model in the future.

**Acknowledgments** This work was supported by the National Natural Science Foundation of China (Grant Nos. 41072238) and the National Natural Science Foundation International Cooperation Projects of China (Grant Nos. 50720135906).

## References

1. Anderson MB, Garrad AD, Hassan U (1984) Teeter excursions of a two-bladed horizontal-axis wind-turbine rotor in a turbulent velocity field. J Wind Eng Ind Aerodyn 17(1):71–88
2. Balabel A, El-Askary WA (2011) On the performance of linear and nonlinear $k - \varepsilon$ turbulence models in various jet flow applications. Eur J Mech B Fluids 30(3):325–340
3. Bazargan M, Mohseni M (2012) Algebraic zero-equation versus complex two-equation turbulence modeling in supercritical fluid flows. Comput Fluids 60:49–57
4. Bejan A (1993) Heat transfer. Wiley, New York
5. Blay D, Mergui S, Niculae C (1992) Confined turbulent mixed convection in the presence of a horizontal buoyant wall jet. Fundam Mix Convect HTD 213:65–72
6. Bukhari SJK, Siddiquia K (2008) An experimental study of the airside flow structure during natural convection. Phys Fluids 20(12):1–11
7. Chen Q (1995) Comparison of different k-ε models for indoor air flow computations. Numer Heat Transf B Fundam 28(3):353–369
8. Comini G, Del Guidice S, Lewis RW, Zienkiewicz OC (1974) Finite element solution of nonlinear heat conduction problems with special reference to phase change. Int J Numer Methods Eng 8:613–624
9. Defraeye T, Blocken B, Carmeliet J (2010) CFD analysis of convective heat transfer at the surfaces of a cube immersed in a turbulent boundary layer. Int J Heat Mass Transf 53:297–308
10. Ezzouhri R, Joubert P, Penot F, Mergui Sophie (2009) Large Eddy simulation of turbulent mixed convection in a 3D ventilated cavity: comparison with existing data. Int J Therm Sci 48: 2017–2024
11. Germano M, Piomelli U, Moin P, Cabot WH (1991) A dynamic subgrid-scale eddy viscosity model. J Phys Fluids A 3:1760–1765
12. Hagishima A, Tanimoto J (2003) Field measurements for estimating the convective heat transfer coefficient at building surfaces. Build Environ 38(7):873–881
13. Harlan RL (1973) Analysis of coupled heat-fluid transport in partially frozen soil. Water Resour Res 9:1314–1323
14. He CX, Wu ZW (1996) Preliminary prediction for the freezing–thawing situation in rock surrounding DabanShan tunnel. In: The dissertations of the fifth national conference on glaciology and geocryology. Culture Press of Gansu, LanZhou, pp 419–425
15. Ilinca F, Pelletier D, Garon A (1997) An adaptive finite element method for a two-equation turbulence model in wall-bounded flows, Internat. J Numer Methods Fluids 24:101–120
16. Kalitzin G, Medic G, Iaccarino G, Durbin Paul (2005) Near-wall behavior of RANS turbulence models and implications for wall functions. J Comput Phys 204:265–291
17. Lacasse D, Turgeon É, Pelletier D (2004) On the judicious use of the k-ε model, wall functions and adaptivity. Int J Therm Sci 43:925–938
18. Lai YM, Wu ZW, Zhu YL, Zhu LN (1999) Nonlinear analysis for the coupled problem of temperature and seepage fields in cold-region tunnels. Cold Reg Sci Technol 29:89–96
19. Lai YM, Wu ZW, Zhu YL, Zhu LN (1998) Nonlinear analysis for the coupled problem of temperature, seepage and stress fields in cold-region tunnels. Tunn Undergr Space Technol 13:435–436
20. Launder BE (1991) Current capabilities for modeling turbulence in industrial flows. Appl Sci Res 48:247–269

21. Lilly DK (1992) A proposed modification of the Germano subgrid-scale closure method. J Phys Fluids A 4:633–635
22. Liu Y, Harris DJ (2007) Full-scale measurements of convective coefficient on external surface of a low-rise building in sheltered conditions. Build Environ 42(7):2718–2736
23. Lotfi R, Saboohi Y, Rashidi AM (2010) Numerical study of forced convective heat transfer of nanofluids: comparison of different approaches. Int Commun Heat Mass Transf 37:74–78
24. Loveday DL, Taki AH (1996) Convective heat transfer coefficients at a plane surface on a full-scale building façade. Int J Heat Mass Transf 39(8):1729–1742
25. Ng KC, Abdul Aziz MA, Ng EYK (2011) On the effect of turbulent intensity towards the accuracy of the zero-equation turbulence model for indoor airflow application. Build Environ 46(1):82–88
26. Nielsen PV, Restivo A, Whitelaw JH (1978) The velocity characteristics of ventilated room. ASME J Fluids Eng 100:291–298
27. Pelletier D, Ignat L, Ilinca F (1997) Adaptive finite element method for conjugate heat transfer. Numer Heat Transf A 32(3):267–287
28. Rodi W, Ferziger JH, Breuer M, Pourquie M (1997) Status of large eddy simulation: results of a workshop. ASME J Fluids Eng 119:248–262
29. Tan XJ, Chen WZ, Tian HM, Cao JJ (2011) Water flow and heat transport including ice/water phase change in porous media: numerical simulation and application. Cold Reg Sci Technol 68(1):74–84
30. Turgeon É, Pelletier D, Ignat L (2000) Effects of adaptivity on various finite element schemes for turbulent heat transfer and flow predictions. Numer Heat Transf A 38:847–868
31. Wijeysundera NE, Chou SK, Jayamaha SEG (1993) Heat flow from walls under transient rain conditions. J Therm Insul Build Envel 17:118–143
32. Zhang W, Chen QY (2000) Large eddy simulation of indoor airflow with a filtered dynamic subgrid scale model. Int J Heat Mass Transf 43:3219–3231
33. Zhang XF, Lai YM, Yu WB, Zhang SJ (2002) Nonlinear analysis for the three-dimensional temperature fields in cold region tunnels. Cold Reg Sci Technol 35:207–219
34. Zhang XF, Lai YM, Yu WB, Zhang SJ, Xiao JZ (2004) Forecast analysis of the refreezing of Kunlun mountain permafrost tunnel on Qing–Tibet railway in China. Cold Reg Sci Technol 39:19–31